Electron-density-sensitive Line Ratios of Fe XIII– XVI from Laboratory Sources Compared to CHIANTI

M. E. Weller[1], P. Beiersdorfer[1] , V. A. Soukhanovskii[1], F. Scotti[1], and B. P. LeBlanc[2]
[1] Lawrence Livermore National Laboratory, Livermore, CA 94550, USA
[2] Princeton Plasma Physics Laboratory, Princeton, NJ 08543, USA

Abstract

We present electron-density-sensitive line ratios for Fe XIII– XVI measured in the spectral wavelength range of 200–440 Å and an electron density range of $(1–4) \times 10^{13} \, \mathrm{cm}^{-3}$. The results provide a test at the high-density limit of density-sensitive line ratios useful for astrophysical studies. The measurements were performed on the National Spherical Torus Experiment-Upgrade, where electron densities were measured independently by the laser Thomson scattering diagnostic. Spectra were collected with a flat-field grazing-incidence spectrometer, which provided a spectral resolution of up to 0.3 Å, i.e., high resolution across the broad wavelength range. The response of the instrument was relatively calibrated using spectroscopic techniques in order to improve accuracy. The line ratios are compared to other laboratory sources and the latest version of CHIANTI (8.0.2), and an agreement within 30% is found.

Key words: atomic data – plasmas – stars: flare – Sun: UV radiation – techniques: spectroscopic – ultraviolet: stars

1. Introduction

The spectrum of iron emission lines in the extreme ultraviolet (EUV) region has provided vital information on the differential emission measure, as well as on the electron density (n_e) of solar and stellar coronal plasma. For example, a comprehensive study of iron emission lines was performed by Brickhouse et al. (1995) with the high-resolution spectra from the Solar Extreme-Ultraviolet Research Telescope and Spectrograph (SERTS; Thomas & Neupert 1994) and from the *Extreme Ultraviolet Explorer* (*EUVE*; Welsh et al. 1990), which measured spectra from a solar active region ($n_e \approx 10^{10} \, \mathrm{cm}^{-3}$) and Capella ($n_e \approx 10^{11}–10^{13} \, \mathrm{cm}^{-3}$), respectively. In the region between 170 and 450 Å, at least 90 lines from Fe IX– XVII were shown to exist, making it an excellent region within which to perform line ratio analysis for electron density estimations. Brickhouse & Dupree (1998) also used the Fe lines in spectra from the *EUVE* to derive densities of the binary system 44i Boo. Emission lines from the EUV region have also been observed with the Cosmic Hot Interstellar Plasma Spectrometer (CHIPS, 90–260 Å; Hurwitz et al. 2005; Lepson et al. 2008), the Low-Energy Transmission Grating Spectrometer (LETGS, 6–176 Å) on the *Chandra X-Ray Observatory* (Beiersdorfer et al. 2014a; Brinkman et al. 2001; Beiersdorfer et al. 2015), and the EUV imaging spectrometer (EIS, 170–211 Å and 246–292 Å; Brown et al. 2008; Del Zanna 2012) on *Hinode*. In addition, Keenan et al. have made extensive comparisons of theoretical calculations with the iron emission-line ratios from the high-resolution spectra from SERTS, including Fe XI (Pinfield et al. 2001; Keenan et al. 2005a), Fe XII (Keenan et al. 1996), Fe XIII (Keenan et al. 2007), Fe XV (Keenan et al. 2005b), and Fe XVI (Keenan et al. 2007).

It is essential for all astrophysical measurements to be compared not only to theory, but also to laboratory measurements with independently measured electron densities and temperatures (T_e). To account for this need, laboratory studies of iron emission lines have been performed on electron beam ion trap (EBIT) facilities. For example, emission lines of Fe VII

through Fe X were measured on the Livermore EBIT facilities (Beiersdorfer et al. 1999a), while Liang et al. (2009a, 2009b) presented data from the Heidelberg EBIT (FLASH-EBIT) of Fe VI– XV in the range of 125–265 Å, with densities approximately 7×10^9–$3 \times 10^{10} \, \mathrm{cm}^{-3}$. Yamamoto et al. (2008), using EBIT-II (Chen et al. 2004) and the Large Helical Device (LHD; Motojima et al. 2005), compared Fe XIII line ratios near 200 Å in the range of 2×10^{11} to $10^{13} \, \mathrm{cm}^{-3}$ to the CHIANTI spectral analysis code (Dere et al. 1997; Del Zanna et al. 2015), giving a high-density limit to Fe XIII line ratios that are generally sensitive below approximately $10^{11} \, \mathrm{cm}^{-3}$. Träbert et al. (2014a, 2014b, 2016; Beiersdorfer et al. 2014b; Träbert & Beiersdorfer 2015) reported EBIT measurements for specific iron lines compared to the Atmospheric Imaging Assembly (AIA) on board *the Solar Dynamics Observatory* (*SDO*; Pesnell et al. 2012). Density-sensitive line ratios were recorded in the Tokyo EBIT (CoBIT) of Fe XIII– XV by Nakamura et al. (2011) and Fe X– XII by Shimizu et al. (2017) in the 160–290 Å range with electron densities near $10^{10} \, \mathrm{cm}^{-3}$. Similarly, density-sensitive line ratios of Fe XXIII were measured by Chen et al. (2004) using the Livermore facilities in the 10^{11}–$10^{12} \, \mathrm{cm}^{-3}$ range.

While EBIT data generally provide line ratios in the electron density range 10^{10}–$10^{11} \, \mathrm{cm}^{-3}$, spectra from magnetic fusion plasma devices can provide ratios for densities in the range 10^{12}–$10^{14} \, \mathrm{cm}^{-3}$. For example, Fournier et al. (2001) measured Fe VIII– XIII lines in the 166–205 Å range for densities $(0.3–3.0) \times 10^{14} \, \mathrm{cm}^{-3}$ on the Frascati Tokamak Upgrade, which showed good agreement with simulations. Lepson et al. (2010) measured line ratios of Fe XXII on the National Spherical Torus Experiment (NSTX) and compared them to calculations performed with the Flexible Atomic Code (FAC; Gu 2008). Lastly, Stratton et al. (1985) measured Fe XVIII– XXII lines in the range 60–200 Å on the Princeton Large Torus tokamak. Those data were recently used in a comparison with spectra from solar flare plasmas (Keenan et al. 2017).

This paper focuses on results from the National Spherical Torus Experiment-Upgrade (NSTX-U; Menard et al. 2012, 2017). In particular, we present Fe XIII–Fe XVI data in the range of 200–440 Å at electron densities ranging between $(1-4) \times 10^{13}$ cm^{-3}. We compare the data to predictions from the latest version of CHIANTI (v. 8.0.2). Section 2 will discuss experimental details and measurements, Section 3 will discuss the relative calibration of the spectrometer response function, and Section 4 will present the results we obtained for Fe XIII– XVI. We will conclude in Section 5.

2. Experimental Setup

The present experiments were performed on NSTX-U during the initial conditioning phase of the machine. Common emission spectra from NSTX-U include carbon (from the graphite walls), helium (from He glow discharges between experiments), boron (from boronization), and oxygen (common impurity in tokamaks). Iron comes from stainless steel components inside NSTX-U, and iron emission generally takes place early on during the experiment (between 0 and 400 ms), usually before good plasma confinement and neutral beam injection (NBI) heating occurs. Nickel and chromium emission lines are also seen in abundance in the EUV wavelength range, though they are considerably weaker than the iron lines. Due to the emission of multiple elements, line blending is an issue, which must be considered when doing any line ratio analysis.

Measurements were taken with the Long-Wavelength Extreme Ultraviolet Spectrometer (LoWEUS), which was developed for tokamak measurements on the Livermore EBITs (Beiersdorfer et al. 1999b; Graf et al. 2008; Lepson et al. 2012). A description of the implementation of LoWEUS on NSTX-U is given by Weller et al. (2016). Briefly, LoWEUS utilizes a flat-field grazing-incidence grating with 1200 lines/mm with a resolution of 0.3 Å FWHM. Indeed, the setup achieves a line width of approximately 0.3 Å near 200 Å, but it is slightly higher at larger wavelengths (approximately 0.5 Å past 300 Å). For the experiments considered in this paper, LoWEUS utilized a Princeton Instruments PIXIS-XO 100B camera that was operated in a "full chip" mode (see Weller et al. 2016 for further details). Although this mode yielded a temporal resolution of only 70 ms per frame, it allowed for an excellent signal-to-noise ratio, which was critical for the line ratio analysis presented in this paper. The spectra we analyze come from four NSXT-U discharges: 204666, 204695, 204737, and 205079, which were chosen due to the "full chip" mode operation of the instruments and quality of the spectra (for most discharges, the instrument was operated in a different mode, which allowed for higher time resolution, but with a cost in signal).

Each NSTX-U discharge has similar start-up conditions, and all data were collected between the times 130–410 ms, depending on the details of the discharge. The average electron density measured with the laser Thomson scattering diagnostic (Diallo et al. 2012) is 3.42 ± 0.33, 1.47 ± 0.12, 1.67 ± 0.08, and $1.94 \pm 0.37 \times 10^{13}$ cm^{-3}, respectively, for the four NSTX-U discharges. The error in the electron density represents the standard deviation of the data. Because we exclude times in which each discharge was heated with NBI, the spectra exhibit little hard X-ray or neutron noise. Soon after plasma initiation, the first iron lines measured are from Fe VII–X. As time progresses and the plasma heats up, iron lines from higher charge states are measured, up to Fe XVI.

Unfortunately, second-order lines dominate above 250 Å, which makes analysis of the data collected from the early part of a given discharge very challenging (Weller et al. 2016). However, when the plasma has heated sufficiently to strip Fe XIII and beyond, very little second-order emission is measured, and reliable analysis of lines measured in first order becomes possible. After the plasma is hot enough to produce Fe XVII, NSTX-U plasma attains good stability and the source of new ions from stainless steel stops. At that point iron radiation essentially disappears. Therefore, there is a brief time in each discharge where the Fe spectra are clean enough to do line ratio analysis, which is approximately 100 ms to 400 ms, after many Fe second-order lines disappear and before NBI turns on and the Fe source dissipates away.

An example spectrum is shown in Figure 1. These data were measured in shot 205079 between 200 and 270 ms. Prominent iron lines are highlighted in black, while lines from all other elements are highlighted in gray, for clarity. In addition in Figure 1, the spectrum is enlarged to show the region between 200–260 Å with most lines identified. It is clear from this figure that many lines are blended.

3. Instrument Calibration

LoWEUS did not undergo an absolute response function calibration; therefore, a relative calibration method utilizing spectroscopic techniques is used. This section describes the details of this process.

Once the data are collected, the spectrum undergoes a background subtraction. This is accomplished by accumulating several dark background frames by triggering the camera several hundred ms before the discharge. These dark frames are then averaged and subtracted from the spectrum. After this subtraction, the wavelength scale must be calibrated. In Figure 1, there are many prominent lines, primarily from C IV and He II, which have well-established wavelength values (we employ reference wavelengths CHIANTI v 8.0.2). Spectra obtained from other time intervals or other NSTX-U shots display lines from O IV– V and N V, which are also used in the calibration. A third-order polynomial fit was performed, which gave agreement to within 0.10 Å of the reference line wavelengths.

The spectral emission later in the discharge, after iron has dissipated away, is dominated by C IV lines, which cover most of the wavelength range and include lines at 222.78, 244.91, 289.23, 312.42, 384.18, and 419.71 Å. The C IV line intensities were determined using a Gaussian fitting program and then compared to the calculated emission strengths given in the CHIANTI database. Thus, our responsivity calibration procedure is similar to that deployed by Lepson et al. (2016) using oxygen lines. The experimentally determined emission strengths were normalized to that of the C IV line at 312.42 Å, which is situated near the center of the wavelength range covered by the instrument. The relative intensities of the C IV lines are nearly insensitive to n_e; however, they are sensitive to T_e. As our measurements integrate over a fixed line of sight, we have no information that we could relate to radial electron temperature measurements. Consequently, we also employed the technique described in Lawson et al. (2009). Their techniques specifically focus on the 3p ^{2}P$_{1/2,3/2} \rightarrow$ 3s ^{2}S$_{1/2}$ lines Ni XVIII (291.98 and 320.56 Å), Fe XVI (335.41 and 360.76 Å), and Cr XIV (389.86 and 412.05 Å) because the lines are insensitive to both n_e and T_e in the NSTX-U parameter

Figure 1. Spectra collected with LoWEUS from NSTX-U discharge 205079 during 200–270 ms. An expanded spectrum is shown below for more clarity. Fe XIII– XVI lines are highlighted in black, while lines from all other elements are in gray.

Figure 2. Responsivity calibration curve based on in situ line ratios and associated spline fits.

range. These lines are reasonably isolated, and can be seen in the data in Figure 1. An iterative process is used to guide the relative calibration curve to a solution, which gives an estimate of C IV emission calculated at T_e equal to 40 eV, which is a

reasonable value. Furthermore, our calibration procedure is augmented by lines from He II, O IV–V, and N V. A spline fit is used to connect the data points with a smooth curve. The fit also assigns errors as a function of wavelength based on the
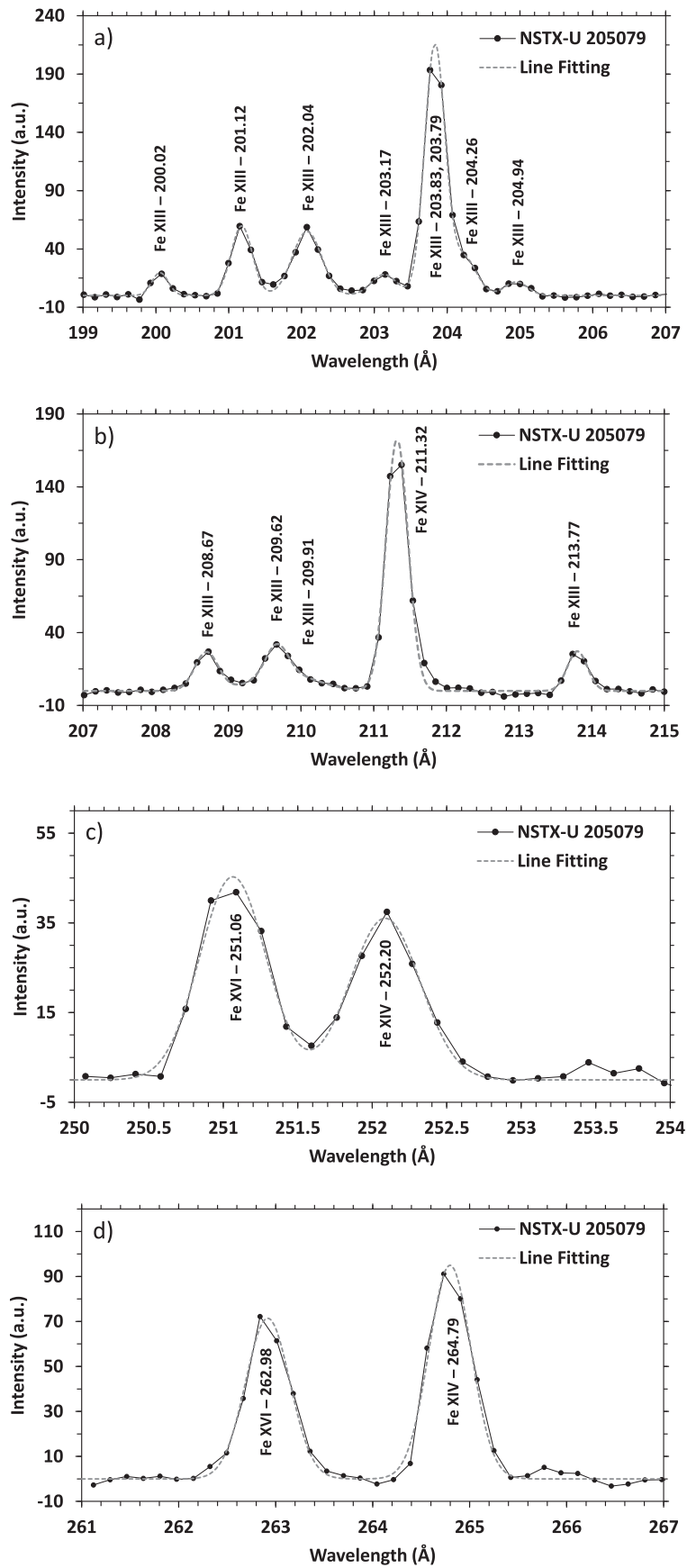
Figure 3. Spectra observed from NSTX-U discharge 205079 and the associated line fits: (a) Fe XIII lines in the range 199–207 Å; (b) Fe XIII lines plus one Fe XIV line in the range 207–215 Å; (c) Fe XVI and Fe XIV line in the range 250–254 Å; (d) Fe XVI and Fe XIV line in the range 261–267 Å.

Table 1
Measured Relative Intensity Values of Fe XIII– XVI Lines in the Wavelength Region 200–440 Å for Four NSTX-U Discharges: 204666, 204695, 204737, and 205079

Ion	Wavelength (Å)	Transition	204666 Intensity (a.u.)	204695 Intensity (a.u.)	204737 Intensity (a.u.)	205079 Intensity (a.u.)
Fe XIII	200.02	$3p3d\ ^3D_2 \rightarrow 3p^2\ ^3P_1$	38.81 ± 5.17	…	17.96 ± 2.56	5.93 ± 0.93
Fe XIII	201.12	$3p3d\ ^3D_1 \rightarrow 3p^2\ ^3P_1$	59.84 ± 5.72	15.31 ± 1.13	30.26 ± 2.88	23.35 ± 1.55
Fe XIII	202.04	$3p3d\ ^3P_1 \rightarrow 3p^2\ ^3P_0$	78.21 ± 6.69	20.19 ± 1.48	43.67 ± 3.69	29.84 ± 1.88
Fe XIII	203.17	$3p3d\ ^3P_0 \rightarrow 3p^2\ ^3P_1$	30.95 ± 5.35	6.59 ± 1.16	9.11 ± 2.25	8.64 ± 1.17
Fe XIII	203.83 (bl)	$3p3d\ ^3D_{3,2} \rightarrow 3p^2\ ^3P_2$	243.49 ± 17.28	55.77 ± 2.53	100.46 ± 13.65	80.91 ± 4.43
Fe XIII	204.26	$3p3d\ ^1D_2 \rightarrow 3p^2\ ^3P_1$	56.23 ± 12.33	8.67 ± 1.16	40.85 ± 12.47	14.78 ± 2.62
Fe XIII	204.94	$3p3d\ ^3D_1 \rightarrow 3p^2\ ^3P_2$	18.72 ± 4.79	5.16 ± 0.93	8.53 ± 2.32	4.95 ± 1.03
Fe XIII	208.67	$3p3d\ ^1P_1 \rightarrow 3p^2\ ^1S_0$	37.11 ± 5.21	9.03 ± 1.32	18.11 ± 3.52	11.43 ± 1.75
Fe XIII	209.62 (bl)	$3p3d\ ^3P_{2,1} \rightarrow 3p^2\ ^3P_{1,2}$	50.09 ± 14.81	13.31 ± 5.41	25.80 ± 9.23	21.95 ± 9.07
Fe XIV	211.32	$3d\ ^2D_{3/2} \rightarrow 3p\ ^2P_{1/2}$	254.03 ± 5.98	20.38 ± 1.04	94.63 ± 6.57	44.57 ± 1.77
Fe XIII	213.77	$3p3d\ ^3P_2 \rightarrow 3p^2\ ^3P_2$	30.07 ± 4.09	5.23 ± 0.94	13.35 ± 2.60	10.02 ± 1.41
Fe XIV	219.13	$3d\ ^2D_{5/2} \rightarrow 3p\ ^2P_{3/2}$	413.91 ± 14.12	34.59 ± 1.31	155.84 ± 9.06	72.83 ± 2.39
Fe XIII	221.83	$3p3d\ ^1D_2 \rightarrow 3p^2\ ^1D_2$	66.19 ± 2.56	12.22 ± 0.60	27.24 ± 1.61	22.03 ± 1.08
Fe XIII	240.70	$3s3p^3\ ^3S_1 \rightarrow 3p^2\ ^3P_0$	16.34 ± 1.27	5.17 ± 0.49	8.93 ± 0.48	9.22 ± 0.66
Fe XV	243.79	$3s3d\ ^1D_2 \rightarrow 3s3p\ ^1P_1$	36.53 ± 0.88	12.92 ± 0.82	19.47 ± 0.85	29.31 ± 1.22
Fe XIII	246.21	$3s3p^3\ ^3S_1 \rightarrow 3p^2\ ^3P_1$	26.57 ± 1.19	5.94 ± 0.66	14.44 ± 1.14	7.88 ± 0.57
Fe XVI	251.06	$3d\ ^2D_{3/2} \rightarrow 3p\ ^2P_{1/2}$	68.03 ± 1.87	16.65 ± 0.64	17.74 ± 0.62	27.19 ± 1.69
Fe XIV	252.20	$3s3p^2\ ^2P_{3/2} \rightarrow 3s^23p\ ^2P_{1/2}$	134.39 ± 6.60	10.56 ± 0.45	58.06 ± 2.47	22.91 ± 1.48
Fe XIV	257.39	$3s3p^2\ ^2P_{1/2} \rightarrow 3s^23p\ ^2P_{1/2}$	74.06 ± 3.63	6.03 ± 0.86	25.65 ± 2.59	15.34 ± 0.86
Fe XIV	258.30	$3p^23d\ ^2F_{7/2} \rightarrow 3s3p3d\ ^2D_{5/2}$	9.35 ± 4.10	…	…	…
Fe XIII	261.74	$3p3d\ ^3F_2 \rightarrow 3p^2\ ^1D_2$	7.97 ± 3.15	…	…	…
Fe XVI	262.98	$3d\ ^2D_{5/2} \rightarrow 3p\ ^2P_{3/2}$	107.76 ± 3.28	24.43 ± 0.80	28.19 ± 1.24	43.12 ± 2.54
Fe XIV	264.79	$3s3p^2\ ^2P_{3/2} \rightarrow 3s^23p\ ^2P_{3/2}$	288.15 ± 7.29	25.61 ± 1.00	106.98 ± 3.41	54.44 ± 2.62
Fe XIV	270.52	$3s3p^2\ ^2P_{1/2} \rightarrow 3s^23p\ ^2P_{3/2}$	89.60 ± 3.31	7.87 ± 0.53	33.23 ± 1.57	16.99 ± 0.90
Fe XIV	274.20	$3s3p^2\ ^2S_{1/2} \rightarrow 3s^23p\ ^2P_{1/2}$	92.56 ± 2.98	8.09 ± 0.51	33.01 ± 1.24	14.99 ± 1.02
Fe XV	284.16	$3s3p\ ^1P_1 \rightarrow 3s^2\ ^1S_0$	399.24 ± 7.39	159.13 ± 4.04	208.09 ± 3.19	342.13 ± 16.88
Fe XIII	318.13	$3s3p^3\ ^1D_2 \rightarrow 3p^2\ ^1D_2$	19.26 ± 1.12	2.92 ± 0.32	9.23 ± 0.64	5.09 ± 0.48
Fe XV	327.02	$3p^2\ ^1D_2 \rightarrow 3s3p\ ^3P_2$	5.39 ± 0.49	2.88 ± 0.45	…	6.33 ± 0.94
Fe XIV	334.17	$3s3p^2\ ^2D_{3/2} \rightarrow 3s^23p\ ^2P_{1/2}$	61.99 ± 9.63	6.03 ± 1.41	18.47 ± 5.27	12.02 ± 0.55
Fe XVI	335.41	$3p\ ^2P_{3/2} \rightarrow 3s\ ^2S_{1/2}$	878.92 ± 20.19	202.70 ± 5.71	241.95 ± 7.50	368.13 ± 14.73
Fe XIV	353.84	$3s3p^2\ ^2D_{5/2} \rightarrow 3s^23p\ ^2P_{3/2}$	96.73 ± 3.37	8.49 ± 0.45	31.37 ± 1.29	17.40 ± 0.91
Fe XIV	358.68	$3p^3\ ^2D_{5/2} \rightarrow 3s3p^2\ ^2D_{5/2}$	15.35 ± 0.84	…	5.76 ± 2.35	…
Fe XVI	360.76	$3p\ ^2P_{1/2} \rightarrow 3s\ ^2S_{1/2}$	456.93 ± 16.16	109.25 ± 3.63	121.91 ± 4.65	192.22 ± 7.26
Fe XV	417.26	$3s3p\ ^3P_1 \rightarrow 3s^2\ ^1S_0$	16.99 ± 2.56	10.69 ± 0.94	…	…

Note. Wavelengths and transitions are included. bl denotes blend; in particular the Fe XIII line at 203.83 Å is blended with the Fe XIII line at 203.79 Å, and the Fe XIII line at 209.62 Å is blended with the Fe XIII line at 209.92 Å.

error associated with each data point. The final calibration is shown in Figure 2. Interestingly, almost no responsivity correction is needed for the first half of the wavelength range covered by LoWEUS. The relative responsivity of the instrument, however, drops sharply at the long wavelengths, which means a large responsivity correction is needed. This relative responsivity curve is a useful tool for doing line ratio analysis, especially of lines that are close together in wavelength; however, there may still be additional errors for lines farther apart, so it should be used with some caution.

4. Results

As mentioned earlier, results were recorded from four NSTX-U discharges. Gaussian line fitting was performed for Fe XIII–XVI lines, and examples are shown in Figure 3. Double Gaussians are used when two lines overlap and can be distinguished in the fitting code. It is important to rule out any possible blending of a given line by lines from other species. For example, the Fe XIII line at

201.13 Å may be blended with an Fe XII line at 201.14 Å, which compromises line ratio results. In this example, Fe XII lines were not found to be a large contributing factor during the time interval during which the spectral data were collected. Even still, many iron emission lines were found to be blended, in particular Fe XV lines. Table 1 gives a summary of the relative intensity results with errors of all the iron emission lines that were not found to be heavily blended and that can potentially be used to do line ratio analysis. The following subsections will highlight the line intensity ratios of Fe XIII, XIV, XV, and XVI and compare them to CHIANTI calculations. Even though a responsivity calibration was performed, we focus our discussion on line ratios between nearby lines to avoid a possible increased error associated with the relative calibration process.

4.1. Fe XIII

Below 250 Å, the spectrum is largely dominated by Fe XIII lines, which are strongly sensitive to electron density in the
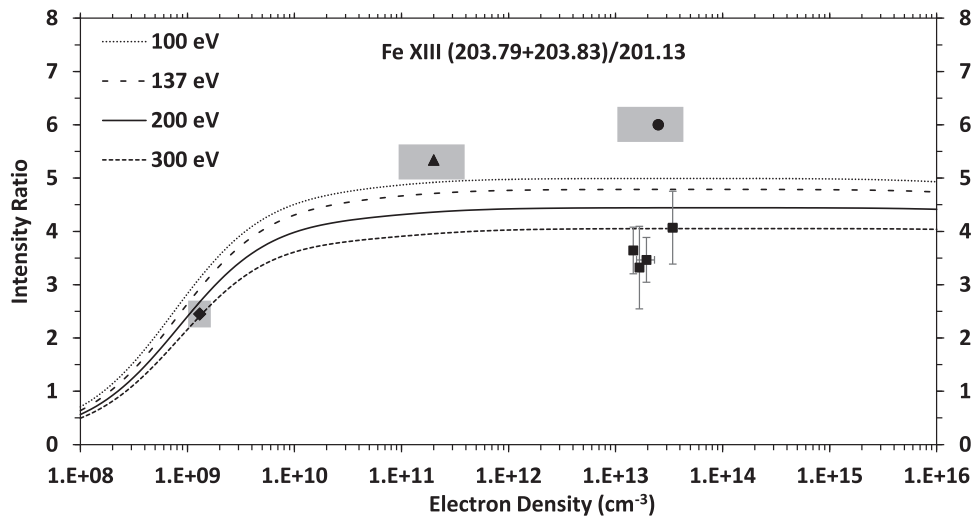
Figure 4. Calculated intensity ratio of Fe XIII lines (203.83+203.79)/201.13 for four different electron temperatures in the electron density range of 10^8–10^{16} cm^{-3} compared to measurements from NSTX-U (black squares), EBIT-II (black triangle; Yamamoto et al. 2008), LHD (black circle; Yamamoto et al. 2008), and FLASH-EBIT (black diamond; Liang et al. 2009a). The shaded areas represent the extent of the measurement uncertainties.
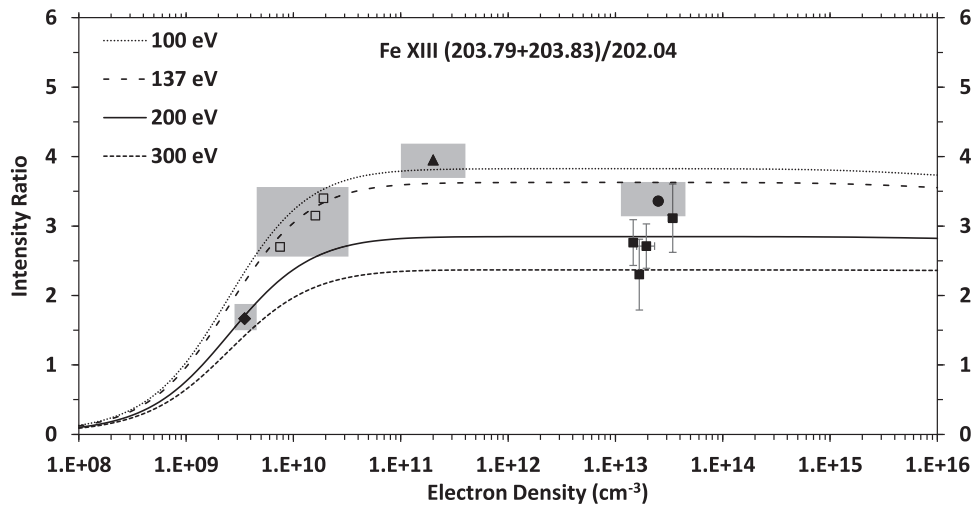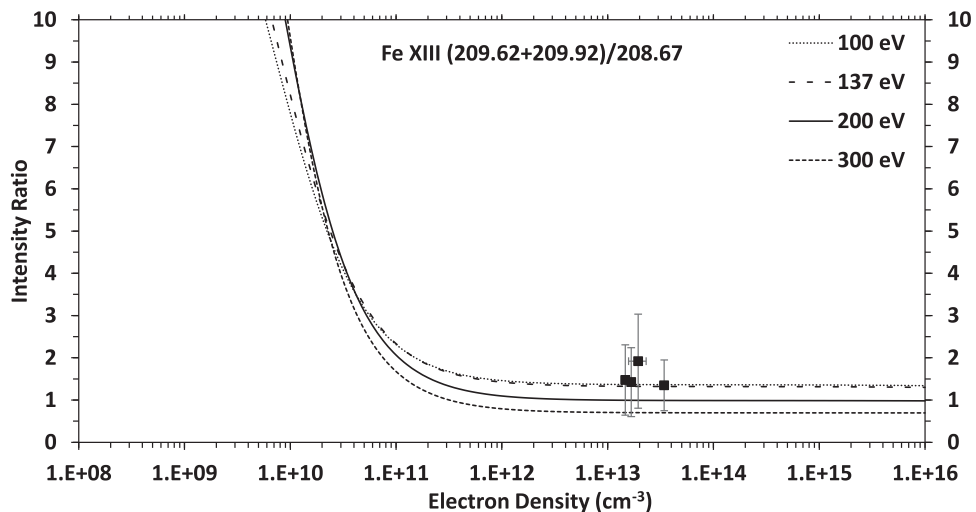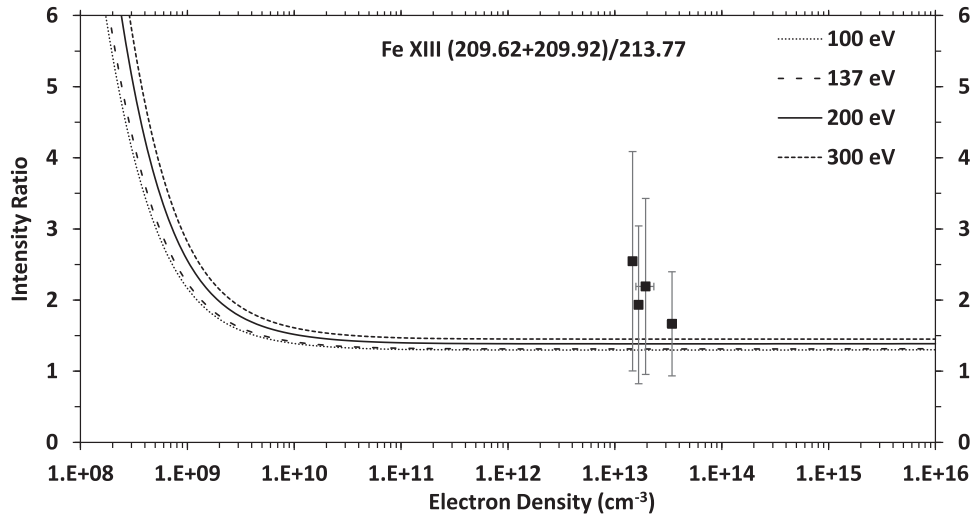

Figure 5. Calculated intensity ratio of Fe XIII lines (203.83 + 203.79)/202.04 for four different electron temperatures in the electron density range of 10^8–10^{16} cm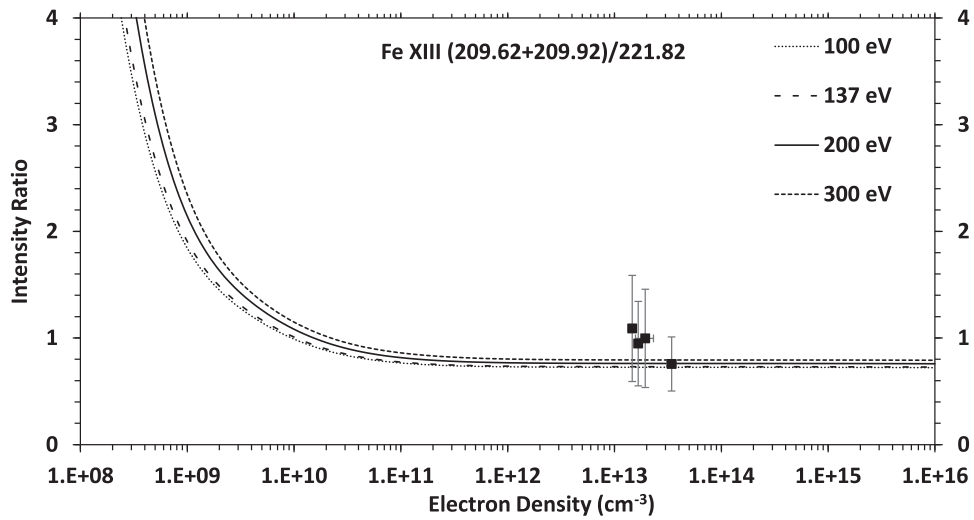$^{-3}$ compared to measurements from NSTX-U (black squares), EBIT-II (black triangle; Yamamoto et al. 2008), LHD (black circle; Yamamoto et al. 2008), FLASH-EBIT (black diamond; Liang et al. 2009a), and CoBIT (white squares; Nakamura et al. 2011). The shaded areas represent the extent of the measurement uncertainties.

Figure 6. Calculated intensity ratio of Fe XIII lines (209.62 + 209.92)/208.67 for four different electron temperatures in the electron density range of 10^8–10^{16} cm^{-3} compared to our measurements from NSTX-U (black squares).

Figure 7. Calculated intensity ratio of Fe XIII lines (209.62 + 209.92)/213.77 for four different electron temperatures in the electron density range of 10^8–10^{16} cm^{-3} compared to our measurements from NSTX-U (black squares).

Figure 8. Calculated intensity ratio of Fe XIII lines (209.62 + 209.92)/221.82 for four different electron temperatures in the electron density range of 10^8–10^{16} cm^{-3} compared to our measurements from NSTX-U (black squares).

10^8–10^{11} cm^{-3} range. Fe XIII is emphasized as being an important density diagnostic for solar plasmas (Flower & Nussbaumer 1974) and has an abundant amount of emission lines in the measured wavelength range (Young et al. 1998). In total, 16 Fe XIII lines are measured and found to be reasonably isolated for analysis. The most intense feature is formed by the blended Fe XIII $3p3d\ ^3D_{3,2} \rightarrow 3p^2\ ^3P_2$ lines at 203.79 and 203.83 Å, and to the long-wavelength side, the Fe XIII $3p3d\ ^1D_2 \rightarrow 3p^2\ ^3P_1$ line at 204.26 Å (see Figure 3(a)). There are many Fe XIII lines close to the left and right of this feature, so it makes for a useful tool. See, for example, Liang et al. (2009a) who reported the line ratio of (203.79 + 203.83)/ (201.13) and compared it with FAC calculations. Figure 4 shows our experimental results for this ratio, in addition to previous results from EBIT-II, LHD, and FLASH-EBIT, and CHIANTI calculations for 100, 137, 200, and 300 eV. The electron temperature of 137 eV is used because it is the temperature of the theoretical maximum abundance of Fe XIII. The electron density dependence of this ratio is flat in the range of NSTX-U densities, and only sensitive to T_e. Our results are in reasonable agreement with CHIANTI calculations. Perhaps

the most heavily reported Fe XIII line ratio, that of (203.79 + 203.83)/(202.04), which is used as a density diagnostic for the solar transition region, is found in Figure 5. In addition to our NSTX-U measurements, laboratory results include those from EBIT-II, LHD, FLASH-EBIT, and CoBIT. This line ratio is found to be very sensitive to T_e with $n_e > 10^{10}$ cm^{-3}, and all four NSTX-U points and the other experimental data lie within the CHIANTI calculations within a reasonable T_e range. An important note to make when comparing EBIT-generated data to tokamak-generated data is that electron-velocity distributions are different, i.e., mono-energetic beam versus Maxwellian distribution. Moreover, tokamak plasma is heavily influenced by transport, which means that ions move to hotter and colder plasma regions where they otherwise would not exist, which is represented by the temperature range that we use in our CHIANTI calculations. This may explain why EBIT and NSTX-U line ratio measurements may indicate different T_e conditions.

The next set of Fe XIII line ratio results focuses on the two blended lines at 209.62 and 209.92 Å (of Figure 3(b)). Results of ratios of these two blended lines with the Fe XIII lines at
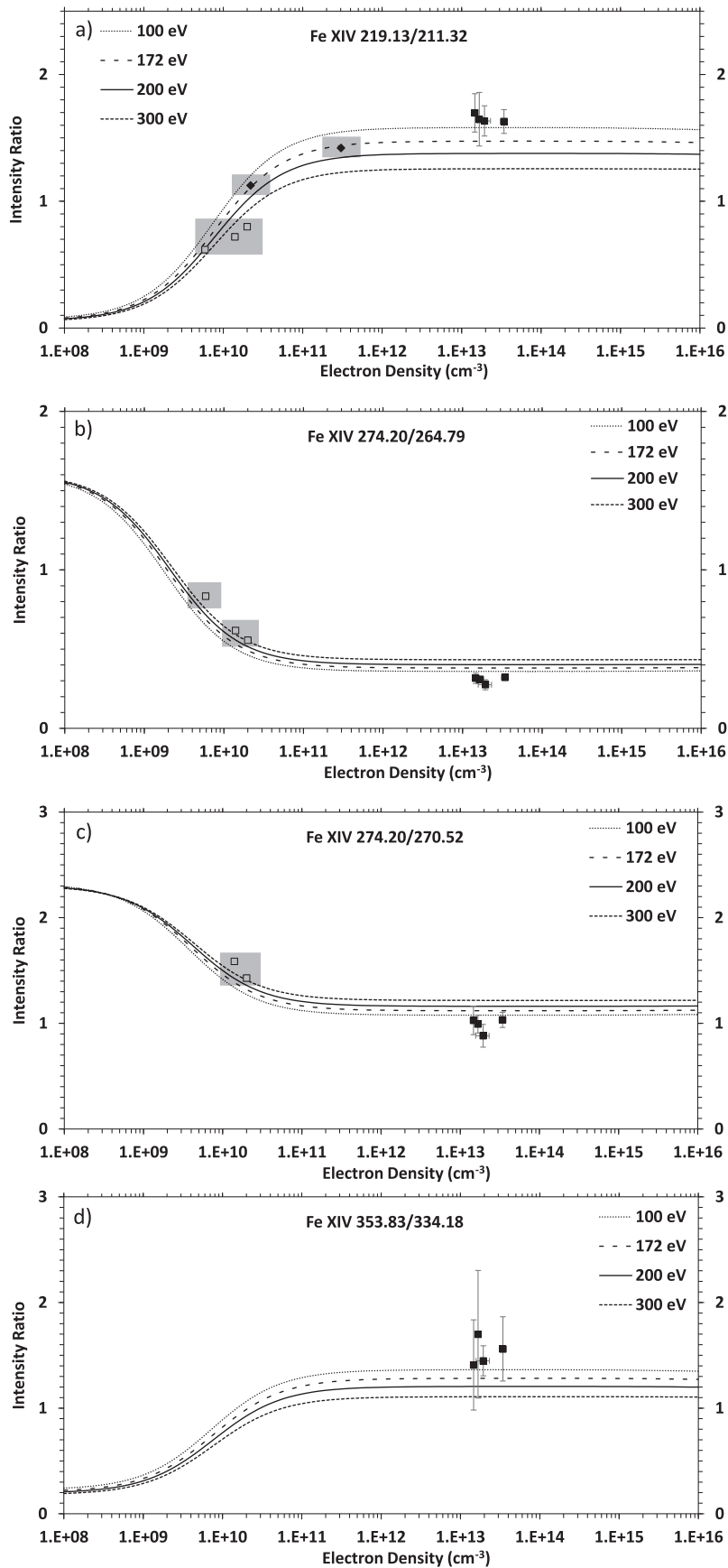
Figure 9. Calculated intensity ratios of Fe XIV lines (a) 219.13/211.32, (b) 274.20/264.79, (c) 274.20/270.52, and (d) 353.83/334.18 for four different electron temperatures in the electron density range of 10^8–10^{16} cm^{-3}. Experimental results are from NSTX-U (black squares), FLASH-EBIT (black diamond; Liang et al. 2009a), and CoBIT (white squares; Nakamura et al. 2011).
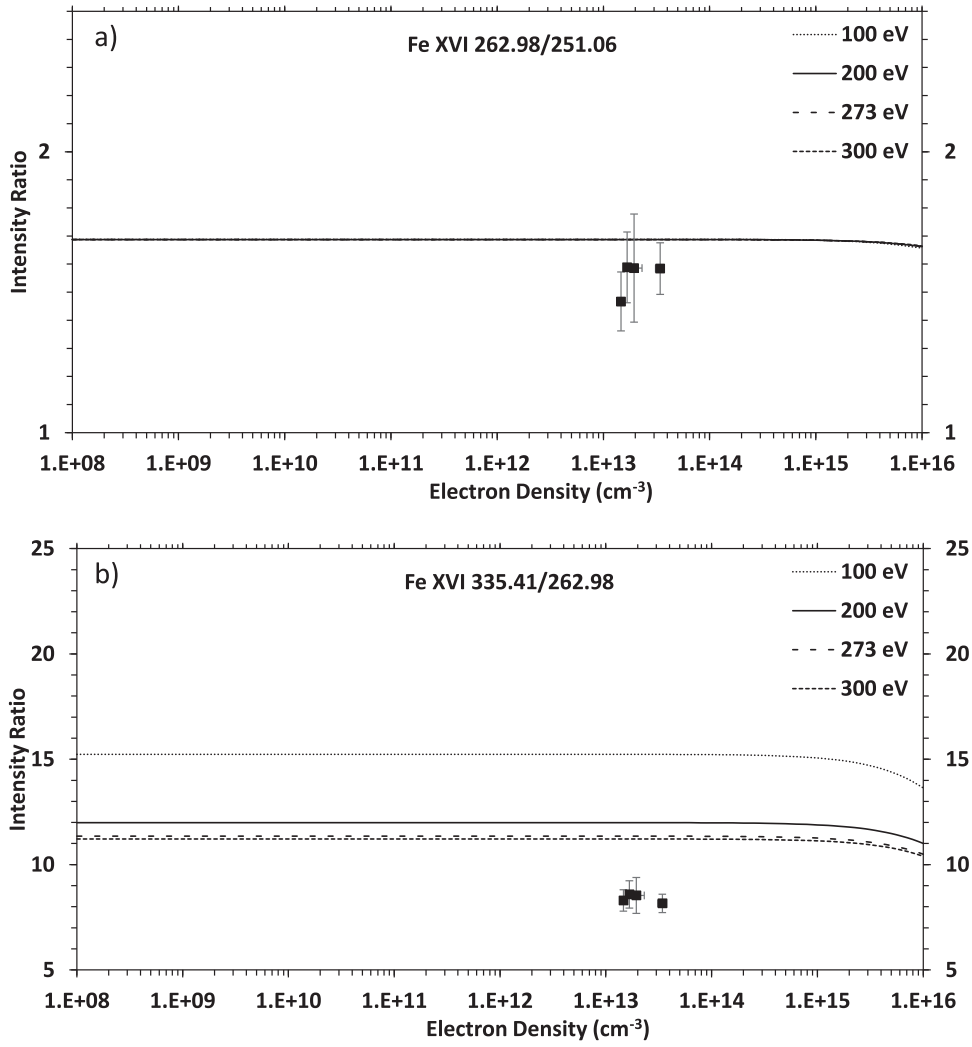
Figure 10. Calculated intensity ratio of Fe XVI lines (a) 262.98/251.06 and (b) 335.41/262.98 for four different electron temperatures in the electron density range of 10^8–10^{16} cm^{-3} compared with our measurements from NSTX-U (black squares).

208.67, 213.77, and 221.82 Å are shown in Figures 6–8, respectively. These line ratios are strongly sensitive to electron density up to 10^{10} cm^{-3} and are not sensitive to T_e, which makes for good high-density limit comparison with CHIANTI calculations. Again, results agree within the spread of plausible temperatures in NSTX-U, although all measured ratios are slightly greater than calculated.

One of the best collections of astrophysical Fe XIII observations is from Landi (2002), and we have used it for line identifications in our spectra. One Fe XIII line that is not included in the Landi paper or found in the NIST Atomic Spectra Database, but is included in the CHIANTI database, is the 3p3d $^3F_2 \rightarrow$ 3p^2 $^1D_2$ transition at 261.74 Å (see more examples of such discrepancies in Beiersdorfer & Lepson 2012). This line is only confirmed for NSTX-U shot 204666, where Fe XIII emission lines were the brightest of the four discharges considered. Other Fe XIII lines, which we have confirmed in our measurements but which we found to be too blended for analysis, were at 216.88, 228.16, 233.23, 239.03, 251.95, 303.36, 311.55, 320.80, 348.18, 359.64, 359.83, 368.16, and 413.00 Å.

4.2. Fe XIV

Fe XIV lines are prevalent throughout the spectrum, and, in total, 11 lines were measured. Key lines that are highlighted are the 3d $^2D_{3/2} \rightarrow$ 3p $^2P_{1/2}$ transition at 211.32 Å, the 3d $^2D_{5/2} \rightarrow$ 3p $^2P_{3/2}$ transition at 219.13 Å, the 3s3p^2 $^2P_{3/2} \rightarrow$ 3s^{2}3p $^2P_{3/2}$ transition at 264.79 Å, the 3s3p^2 $^2P_{1/2} \rightarrow$ 3s^{2}3p $^2P_{3/2}$ transition at 270.52 Å, the 3s3p^2 $^2S_{1/2} \rightarrow$ 3s^{2}3p $^2P_{1/2}$ transition at 274.20 Å, the 3s3p^2 $^2D_{3/2} \rightarrow$ 3s^{2}3p $^2P_{1/2}$ transition at 334.17 Å, and the 3s3p^2 $^2D_{5/2} \rightarrow$ 3s^{2}3p $^2P_{3/2}$ transition at 353.84 Å. Ratios of measured line pairs at 219.13/211.32, 274.20/264.79, 274.20/270.52, and 353.83/334.18 are shown together with those calculated by CHIANTI (100, 172, 200, and 300 eV) in Figure 9. Also shown are FLASH-EBIT and CoBIT results, which are generated at lower electron densities, where the ratios are more sensitive to density. The results agree within the temperature spread in the CHIANTI calculations.

Other possible candidates for a line ratio comparison are the 3s3p^2 $^2P_{1/2,3/2} \rightarrow$ 3s^{2}3p $^2P_{1/2}$ lines at 257.39 and 252.20 Å, both of which are listed in Table 1. However, the line at 252.20 Å is likely blended with an Fe XIII line at 251.95 Å,

which produces results that are off from CHIANTI predictions by approximately 50%. Other Fe XIV lines identified but found to be blended were those at 216.93, 218.17, 218.57, 220.08, 224.35, 225.32, 225.74, 226.04, 240.16, 299.40, and 299.50 Å.

4.3. Fe XV

In total, only four Fe XV lines were confirmed as measured and found to not to be heavily blended, including the most dominant $3s3p\ ^1P_1 \rightarrow 3s^2\ ^1S_0$ line at 284.16 Å. The blended lines that were identified included those at 224.75, 227.20, 227.73, 233.86, 234.78, 242.10, 302.33, 304.89, 305.88, 307.73, 315.34, 315.56, 319.05, 321.77, and 332.85 Å. Historically, the line ratio between the $3s3d\ ^1D_{2,3} \rightarrow 3s3p\ ^1P_{1,2}$ lines at 243.79 Å (listed in Table 1) and 233.86 Å has been used as a good electron density diagnostic. However, the line at 233.86 Å was found to be slightly blended with an Fe XIII line at 233.23 Å and a Ni XVIII line at 233.76 Å, so a direct comparison to theory was not made. The other two Fe XV lines measured were the $3p^2\ ^1D_2 \rightarrow 3s3p\ ^3P_2$ transition at 327.02 Å and the $3s3p\ ^3P_1 \rightarrow 3s^2\ ^1S_0$ transition at 417.26 Å.

4.4. Fe XVI

There are not many Fe XVI emission lines in the 200–440 Å range. Only four were measured, specifically the $3d\ ^2D_{3/2,5/2} \rightarrow 3p\ ^2P_{1/2,3/2}$ lines at 251.02 and 262.98 Å and the $3p\ ^2P_{3/2,1/2} \rightarrow 3s\ ^2S_{1/2}$ lines at 335.41 and 360.76 Å. Both were used in the relative calibration process. Figure 10(a) shows the measured and calculated ratio of (262.98)/(251.02). This ratio was calculated to be insensitive to both n_e and T_e under most conditions, so this ratio can be used as a good check against CHIANTI calculations. The calculated CHIANTI ratio of (262.98)/(251.02) was 1.69, while the measured ratios were found to be 1.58 ± 0.09, 1.47 ± 0.11, 1.59 ± 0.13, and 1.59 ± 0.19. Even though the measured ratios were just under that of the CHIANTI estimate, the difference is still within most of the error bars. Figure 10(b) shows the measured and calculated ratio of (335.41)/(262.98). The measured ratio is approximately 30% lower than that of the highest T_e CHIANTI calculations. This is clearly a significant difference. However, as mentioned at the end of Section 3, unidentified errors for lines far apart may be contributing to this discrepancy.

5. Discussion and Conclusions

Data of density-sensitive Fe XIII– XVI emission lines between 200 and 440 Å in the electron density region of $\sim 10^{13}\ cm^{-3}$ were collected with the high-resolution spectrometer LoWEUS and a relative calibration was performed so that intensity values could be measured. The intensity values were analyzed and line ratios were compared to theoretical calculations given by CHIANTI (8.0.2), as well as compared to other laboratory results. In total, 35 Fe lines were measured for line ratio analysis. At 16, Fe XIII had the most amount of lines for analysis and provided excellent benchmarks for the high-density limit of astrophysically interesting line ratios. For example, the (203.79 + 203.83)/(202.04) line ratio has been used as a tool for electron density estimates for many astrophysical measurements, and the results show that CHIANTI gives good agreement with our data.

Fe XIV lines were also measured in this wavelength range producing four useful line ratios, which agree to CHIANTI calculations. Fe XV proved to be heavily blended; however,

four lines could be measured reliably in the present wavelength range. Fe XVI emission lines are not abundant in this region. However, four lines were measured, and the (335.41)/(262.98) line ratio exhibited the most significant difference with CHIANTI predictions, although these lines are far apart and the implemented calibration may be fraught with unidentified errors.

In summary, results from Fe XIII–XVI ion stages produced in the n_e range of $10^{13}\ cm^{-3}$ show good agreement with CHIANTI calculations (to within 30%), extending previous tests performed with other laboratory devices into a higher density regime.

ORCID iDs

P. Beiersdorfer ⓘ https://orcid.org/0000-0003-0127-599X

References

Beiersdorfer, P., Crespo Lopez-Urrutia, J. R., Springer, P., Utter, S. B., & Wong, K. L. 1999b, RSI, 70, 276
Beiersdorfer, P., Hell, N., Lepson, J. K., Diaz, F., & Ishikawa, Y. 2015, ApJ, 815, 3
Beiersdorfer, P., & Lepson, J. K. 2012, ApJS, 201, 28
Beiersdorfer, P., Lepson, J. K., Brown, G. V., et al. 1999a, ApJL, 519, L185
Beiersdorfer, P., Lepson, J. K., Desai, P., Diaz, F., & Ishikawa, Y. 2014a, ApJS, 210, 16
Beiersdorfer, P., Trabert, E., Lepson, J. K., Brickhouse, N. S., & Golub, L. 2014b, ApJ, 788, 25
Brickhouse, N. S., & Dupree, A. K. 1998, ApJ, 502, 918
Brickhouse, N. S., Raymond, J. C., & Smith, B. W. 1995, ApJS, 97, 551
Brinkman, A. C., Behar, E., Gudel, M., et al. 2001, A&A, 365, L324
Brosius, J. W., Davila, J. M., & Thomas, R. J. 1998, ApJS, 119, 255
Brown, C. M., Feldman, U., Seely, J. F., Korendyke, C. M., & Hara, H. 2008, ApJS, 176, 511
Chen, H., Beiersdorfer, P., Heeter, L. A., et al. 2004, ApJ, 611, 598
Del Zanna, G. 2012, A&A, 537, A38
Del Zanna, G., Dere, K. P., Young, P. R., Landi, E., & Mason, H. E. 2015, A&A, 582, A56
Dere, K. P., Landi, E., Mason, H. E., Monsignori Fossi, B. C., & Young, P. R. 1997, A&AS, 125, 149
Diallo, A., LeBlanc, B. P., Labik, G, & Stevens, D. 2012, RSI, 83, 10D532
Flower, D. R., & Nussbaumer, H. 1974, A&A, 31, 353
Fournier, K. B., Finkenthal, M., Pacella, D., et al. 2001, ApJL, 550, L117
Graf, A. T., Brockington, S., Horton, R., et al. 2008, CaJPh, 86, 307
Gu, M. F. 2008, CaJPh, 86, 675
Hurwitz, M., Sasseen, T. P., & Sirk, M. M. 2005, ApJ, 623, 911
Keenan, F. P., Aggarwal, K. M., Milligan, R. O., et al. 2005b, MNRAS, 356, 1592
Keenan, F. P., Aggarwal, K. M., Ryans, R. S. I., et al. 2005a, ApJ, 624, 428
Keenan, F. P., Jess, D. B., Aggarwal, K. M., et al. 2007, MNRAS, 376, 205
Keenan, F. P., Milligan, R. O., Mathioudakis, M., & Christian, D. J. 2017, MNRAS, 468, 1117
Keenan, F. P., Thomas, R. J., Neupert, W. M., et al. 1996, MNRAS, 278, 773
Landi, E. 2002, A&A, 382, 1106
Lawson, K. D., Zacks, J., Coffey, I. H., & JET-EFDA Contributors 2009, EFDA-JET-R(09)01, http://www.euro-fusionscipub.org/wp-content/uploads/2014/11/EFDR09001.pdf
Lepson, J. K., Beiersdorfer, P., Clementson, J., et al. 2010, JPhB, 43, 144018
Lepson, J. K., Beiersdorfer, P., Clementson, J., et al. 2012, RSI, 83, 10D520
Lepson, J. K., Beiersdorfer, P., Hurwitz, M., et al. 2008, JPhCS, 130, 012014

Lepson, J. K., Beiersdorfer, P., Kaita, R., Majeski, R., & Boyle, D. 2016, RSI, 87, 11D614

Liang, G. Y., Baumann, T. M., Crespo Lopez-Urrutia, J. R., et al. 2009a, ApJ, 696, 2275

Liang, G. Y., Crespo Lopez-Urrutia, J. R., Baumann, T. M., et al. 2009b, ApJ, 702, 838

Menard, J. E., Allain, J. P., Battaglia, D. J., et al. 2017, NucFu, 57, 102006

Menard, J. E., Gerhardt, S., Bell, M., et al. 2012, NucFu, 52, 083015

Motojima, O., Ida, K., Watanabe, K. Y., et al. 2005, NucFu, 45, 255

Nakamura, N., Watanabe, E., Sakaue, H. A., et al. 2011, ApJ, 739, 17

Pesnell, W. D., Thompson, B. J., & Chamberlin, P. C. 2012, SoPh, 275, 3

Pinfield, D. J., Keenan, F. P., Mathioudakis, M., et al. 2001, ApJ, 562, 566

Shimizu, E., Ali, S., Tsuda, T., et al. 2017, A&A, 601, A111

Stratton, B. C., Moos, H. W., Suckewer, S., et al. 1985, PhRvA, 31, 2534

Thomas, R. J., & Neupert, W. M. 1994, ApJS, 91, 461

Träbert, E., & Beiersdorfer, P. 2015, JPhCS, 583, 012008

Träbert, E., Beiersdorfer, P., Brickhouse, N. S., & Golub, L. 2014a, ApJS, 211, 1

Träbert, E., Beiersdorfer, P., Brickhouse, N. S., & Golub, L. 2014b, ApJS, 215, 6

Träbert, E., Beiersdorfer, P., Brickhouse, N. S., & Golub, L. 2016, A&A, 586, A115

Weller, M. E., Beiersdorfer, P., Soukhanovskii, V. A., Magee, E. W., & Scotti, F. 2016, RSI, 87, 11E324

Welsh, B. Y., Vallerga, J. V., Jelinsky, P. N., et al. 1990, OptEn, 29, 752

Yamamoto, N., Kato, T., Funaba, H., et al. 2008, ApJ, 689, 646

Young, P. R., Landi, E., & Thomas, R. J. 1998, A&A, 329, 291